ADVANCED FUNCTIONAL MATERIALS
www.afm-journal.de

3D Printed Ultra-Fast Plastic Scintillators Based on Perovskite-Photocurable Polymer Composite

Antonella Giuri, Amal C Chekkallur, Mario Calora, Rosanna Mastria, Loris Martinazzoli, Etiennette Auffray, Sanosh Kunjalukkal Padmanabhan, Sara Carturan, Sandra Moretto, Gianluca Quarta, Lucio Calcagnile, Matteo Polo, Alberto Quaranta, Alfonso Maffezzoli, Anna Paola Caricato, Aurora Rizzo, and Carola Esposito Corcione**

Additive manufacturing technology is exploited for the first time to build a complex geometry scintillator using a thermosetting photocurable resin filled by lead halide perovskite as an active material. To this aim, an innovative nanocomposite is developed based on Cs_4PbBr_6 perovskite powders as fillers and photocurable resin as matrix, adopting stereolithography as a manufacturing process. The use of high-Z lead-based perovskite filler is needed for the detection of ionizing radiation and the conversion into visible light, while the polymer matrix provides 3D printability. On the one hand, the inclusion of the perovskite-based filler in the photocurable resin does not affect the rheological behavior and photocuring properties of the polymer matrix, making the composite suitable for 3D printing by stereolithography. On the other hand, the presence of the polymer does not affect the emission properties of the perovskite leading to the development of a fast response scintillator with significantly improved environmental stability. This work opens the avenue to the development of a completely new class of plastic scintillating materials.

1. Introduction

Radiation detection is an important aspect in many fields such as high energy physics, medical imaging, homeland security etc.[1–3] Scintillation detectors, among various types of radiation detectors, offer the highest versatility in terms of operating modes, detectable radiation types, and energy range.[4]

Scintillators are materials capable of converting high-energy photons (e.g., X-ray or gamma-ray) or particles (e.g., electrons, protons, neutrons, or heavy ions) into UV-visible (UV-vis) light.[5–7] Several crucial parameters govern scintillation-based detection systems including scintillation light yield, stopping power, decay times, energy resolution, and radiation hardness.[5] The

A. Giuri, A. C Chekkallur, M. Calora, R. Mastria, A. Rizzo
CNR nanotec Istituto di Nanotecnologia
c/o Campus Ecotekne, Via Monteroni, Lecce 73100, Italy
E-mail: antonella.giuri@nanotec.cnr.it

A. C Chekkallur, S. K. Padmanabhan, A. Maffezzoli, C. Esposito Corcione
Dipartimento di Ingegneria dell'Innovazione
Università del Salento
via per Monteroni, km 1, Lecce 73100, Italy
E-mail: carola.corcione@unisalento.it

A. C Chekkallur, M. Calora, G. Quarta, L. Calcagnile, A. P. Caricato, A. Rizzo, C. Esposito Corcione
National Institute of Nuclear Physics (INFN)-Lecce Section
via per Monteroni, km 1, Lecce 73100, Italy

M. Calora, A. P. Caricato
Dipartimento di Matematica e Fisica "E. De Giorgi"
Universià del Salento
via Arnesano, Lecce 73100, Italy

The ORCID identification number(s) for the author(s) of this article can be found under https://doi.org/10.1002/adfm.202417653

L. Martinazzoli, E. Auffray
European Organization for Nuclear Research (CERN)
Geneva 1211–23, Switzerland

S. Carturan, S. Moretto
Department of Physics and Astronomy "Galileo Galilei"
Via Marzolo, Padova 8–35131, Italy

S. Carturan, S. Moretto
INFN Legnaro National Laboratories
Viale dell'Università, 2, Legnaro (PD) 35020, Italy

G. Quarta, L. Calcagnile
CEDAD (Centre of Applied Physics, Dating and Diagnostics)
Department of Mathematics and Physics "Ennio de Giorgi"-University of Salento
via per Monteroni, km 1, Lecce 73100

M. Polo, A. Quaranta
Dipartimento di Ingegneria industriale
Università di Trento
via Sommarive 9 Trento 38123, Italy

M. Polo, A. Quaranta
INFN TIFPA
Trento Institute for Fundamental Physics and Applications
Via Sommarive 14, Povo, Trento 38123, Italy

DOI: 10.1002/adfm.202417653

composition of atomic constituents within a scintillator significantly exerts a profound influence on its radioluminescence process, primarily due to the exponential increase in X-ray absorption with atomic number. In fact, the probability of interaction with ionizing radiation follows a power law dependence on the effective atomic number, Z, of the scintillating material ($\propto Z^n$, where n can vary from 1 to 5 depending on the type of interaction).[8] While a variety of scintillation materials containing heavy atoms have been extensively characterized for efficient X-ray scintillation, the majority of these materials exist as bulk crystals grown using the Czochralski or Bridgman method at temperatures exceeding often 1700 °C, which is a quite long and expensive procedure.

In this scenario, plastic scintillators consisting of a polymer matrix and a fluorescent dye with energy levels compatible with the matrix for efficient energy coupling are very attractive.[8,9] They represent a cost-effective and easy-to-make alternative to the conventional inorganic scintillator detectors and can also be widely applied in particle physics due to their excellent particle identification, tracking capabilities, and time resolution.

Yet, addressing new experimental needs and enhancing performance requires the construction of complex detector geometries that are a challenging target using current production techniques.[10] For instance, in radiotherapy, there is a growing demand for scintillators for volumetric and real-time (4D) beam monitoring and dosimetry detectors. Modern approaches utilize intensity-modulated and volumetric-modulated therapies for high conformity, involving irregularly shaped radiation fields and steep dose gradients. Hence, real-time verification of the delivered dose distribution is essential. Patient alignment and motion pose additional challenges in dose delivery control, leading to the development of phantoms simulating real patient behavior during irradiation.

Traditionally, plastic scintillators are produced by thermal polymerization, a process that can take several hours or even days. In addition, the scintillators produced tend to have regular geometric shapes, such as slabs cylinders, or fibers, which limits their adaptability to more complex geometries. They also have certain limitations, such as relatively low light yield, low radiation hardness, and limited effective atomic number (Z_{eff}).

Despite enormous efforts, the development of scintillating materials at low-temperature suitable for mass production, fast, highly sensitive to X and gamma rays with complex shapes remains a challenging task.

More recently, additive manufacturing (AM) techniques, have been applied as a tool for fabricating volumetric plastic scintillators with specific and complex geometries, broadening the potential applications of plastic scintillators.[11–15] However, in comparison to inorganic materials, polymers inherently exhibit lower density and Z values. Due to the difficulty of incorporating heavy elements directly into the polymer chain, the introduction of high-Z particles as fillers, such as inorganic crystals, represents a possible alternative approach.[8,9,16] The loading of high-Z constituents can significantly enhance the scintillating capabilities of polymers, making them suitable for applications such as gamma spectroscopy.[17–19]

Given the exceptional photophysical properties[20,21] and the presence of high-Z ions (such as Pb, Bi, and I) in their composition, Metal Halide Perovskites (MHPs) have recently garnered the first significant interest as scintillating materials. These materials exhibit high photon attenuation, fast and efficient emission properties,[6,7,21,22] and extreme radiation hardness.[23]

In a recent study, the efficient sensitization of a plastic scintillator with $CsPbBr_3$ MHP nanocrystals NCs has been demonstrated, achieving highly stable radioluminescence with an efficiency comparable to that of commercial-grade inorganic and plastic scintillators.[24,25] Additionally, several embedding strategies are proposed[26] but the 3D printing of plastic scintillators with metal halide perovskite fillers has never been attempted before.

In this study, a 3D printable polymer-based nanocomposite filled with all-inorganic MHP as scintillating material has been developed for the first time. The nanocomposite can be conveniently printed via Stereolithography (SLA), an AM technology, with the aim of creating scintillators with customized geometries, improved stability in ambient air, and a fast response time. The SLA technique indeed allows building objects by solidifying layer-by-layer a liquid resin through photopolymerization reaction, driven by UV irradiation, and has gained significant attention thanks to its ability to accurately produce objects with quite complex geometries[27–29] The innovative photocurable formulations, are obtained by incorporating all-inorganic lead halide perovskite Cs_4PbBr_6 powders into SLA-compatible formulation, which is adopted as photoreactive organic phase in the composite. The MHP radiation-sensitive filler from its part is used to convert high-energy radiations into visible light. Perovskite is characterized by high photoluminescence quantum yields (PLQYs), narrow emission line width, wide emission spectra tunability, and low material cost.[30–33] Among the different results, the present work demonstrates that the photo-curing properties of the photocurable resin are unaltered by the addition of the filler (Cs_4PbBr_6), and the stability of Cs_4PbBr_6 is significantly improved in the composite. The newly developed formulations are applied in stereolithography, enabling the creation of state-of-the-art scintillating materials with advanced geometries. This paper proposes a new approach to the fabrication of scintillators that can be used in intensity-modulated and volume-modulated therapies for high conformity, with irregularly shaped radiation fields for real-time verification of the dose distribution delivered by radiotherapy.

2. Experimental Section

2.1. Materials

In this paper, the following materials have been used. A UV-curable acrylic-based resin known as "GENESIS-Development Resin Base" (GDRB), produced by Thethon 3D, was selected because it is suitable for developing new UV-curing resin formulations for stereolithography by fillers inclusion. The photo-initiator present in the UV resin is (2,4,6-Trimethylbenzoyl)diphenylphosphine Oxide, and its maximum absorption peak is reported to be at 365 nm. A synthesized metal halide perovskites Cs_4PbBr_6 powder was added to the GDRB resin to evaluate the printability of the composite formulation to produce plastic scintillators by stereolithography. The synthesis of the powder was performed following the recipe reported in

Table 1. Composite formulations: ID and composition.

Sample identification code	Weight % of the filler in relation to the GDRB
Cs_4PbBr_6 (0.25%)-GDRB	0.25
Cs_4PbBr_6 (0.5%)-GDRB	0.5
Cs_4PbBr_6 (1%)-GDRB	1
Cs_4PbBr_6 (2.5%)-GDRB	2.5
Cs_4PbBr_6 (10%)-GDRB	10
Cs_4PbBr_6 (30%)-GDRB	30

the reference[31] with some modifications, i.e., the antisolvent used was a mixture of 3% of water in tetrahydrofuran.

2.2. Methods

2.2.1. Powder Characterization

The size of the perovskite particles was measured using a dynamic light scattering (DLS) analysis (Zetasizer Nano ZS90, Malvern Instruments, Worcestershire, U.K.). For the analysis, perovskite particles were dispersed in Tetrahydrofuran (THF) by sonication, and quartz cuvettes were used as the sample cells.

2.2.2. Composite Formulation

Composite formulations, incorporating Cs_4PbBr_6 at concentrations ranging from 0.25 to 30 wt.% with respect to GENESIS-DRB (GDRB) resin, were formulated within a glovebox under a nitrogen atmosphere. The detailed compositions of all the formulations with the respective identification codes can be found in **Table 1**.

The *rheological analysis* of the nanocomposite formulation was performed using a Malvern Kinexus Pro+ strain-controlled rheometer equipped with a parallel plate geometry (radius = 12.5 mm) in steady-state mode with a gap of 0.4 and a shear rate range from 0.1 to 1000 s^{-1} at room temperature (RT). Tests were performed in triplicate and the average curve was plotted for each composition.

Fourier transform infrared (FTIR) measurements were conducted using a Jasco FT/IR 6300 spectrometer. The measurements were taken at 15-min intervals while exposing the samples to UV radiation for a total duration of 60 min to evaluate the degree of cure. The conversion percentage, χ, was calculated by taking the area of absorbance peaks, A^i_j, of —C ═C band at 1636 cm^{-1}, in comparison to those of the reference band (1533 cm^{-1} CO—NH) not affected by the polymerization, according to the following equation:

$$\chi\ (t) = \frac{\frac{A^f_0}{A^r_0} - \frac{A^f_t}{A^r_t}}{\frac{A^f_0}{A^r_0}} \times 100 \quad (1)$$

where A_0 is the area of absorbance peak at time t = 0 and A_t is the area of the absorbance peak at the time t after UV irradiation. Superscript f refers to the peak at 1636 cm^{-1} of the functional group and superscript r to the peak 1533 cm^{-1} of the reference group.

2.2.3. Sample Fabrication

The nanocomposite formulations were first converted into thin films using a doctor blade on an aluminum substrate, achieving a thickness ranging from 150 to 300 µm. Subsequently, the films underwent polymerization by UV exposure using a UV lamp (Spectroline-MODEL ENF-280C/FE, 230 V, 50 Hz, 0.17 A, equipped with a filter) with a peak wavelength of 365 nm. The curing process took place inside a glovebox under a nitrogen atmosphere for a duration of 120 min.

For the scintillation tests, cylinders of 2 mm height and 1 cm diameter were made by drop casting the liquid formulation into cylindrical PDMS moulds, UV cured inside a glovebox under a nitrogen atmosphere for a duration of 180 min.

2.2.4. Morphological/Structural Characterisation

Scanning Electron Microscopy (SEM) analysis of the nanocomposite films was performed by a FESEM microscope Zeiss Sigma 300 VP, using a GEMINI technology and an applied acceleration voltage of 5 and 10 kV. ImageJ software was used to analyze the SEM images and to measure the particle size of Cs_4PbBr_6 inside the resin.

The X-Ray diffraction (XRD) measurements for the Cs_4PbBr_6 powder and Cs_4PbBr6-GDRB thin films were taken using a Rigaku Ultima IV- Diffractometer with a fixed monochromator in $2\theta/\theta$ scanning mode. A Cu K-α X-Ray source of 40 kV with 20 mA current source was used to determine the crystallographic structure and to study the effect of aging in the crystal structure of Cs_4PbBr_6 perovskite before and after inclusion in the polymeric matrix of GDRB.

2.2.5. Photo-Physical Analysis

Optical properties of the perovskite powder and nanocomposite: The optical characterizations were carried out on perovskite Cs_4PbBr_6 powders confined by two glass substrates and on Cs_4PbBr6/GDRB thin films, fabricated as explained above. The UV–vis spectra of the samples were obtained with a double beam spectrophotometer UV–Vis–Nir Perkin Elmer Lambda 950, equipped with the integrating sphere. One beam was used as the reference (absorbance of the glass substrate); the other beam passed through the sample (perovskite powders). For Cs_4PbBr_6-GDRB thin film analysis, one beam was used as a reference (air), and the other beam passed through the sample without any support (Cs_4PbBr_6-GDRB thin films). Data were collected from 250 to 800 nm in absorbance mode with 4 nm steps and the use of an integrated sphere. The photoluminescence (PL) measurements were recorded by means of an Edinburgh FLS980 spectrometer, equipped with a laser diode as an excitation source in continuous mode and double grating excitation and emission monochromators. All the optical measurements were performed at room temperature on perovskite powders confined

by two glass substrates or on Cs_4PbBr_6-GDRB thin films. The PL emission spectra were recorded by using an excitation wavelength of 375 nm and data were collected from 450 to 600 nm with an emission band-pass filter at 425 nm. Emission lifetimes in the ps-ns range were determined with the Time-correlated Single Photon Counting (TCSPC) technique by means of Edinburgh FLS980 spectrometer using a laser diode as excitation source (1 MHz, λexc = 407/550/630 nm–200 ps pulse resolution) and a Hamamatsu MCP R3809U-50 (time resolution 20 ps) as detector. Analysis of the luminescence decay profiles versus time was accomplished with the Decay Analysis Software provided by the manufacturer.

Ionizing radiation measurements: Ion Beam Induced Luminescence (IBIL) measurements were performed at the external beam set-up available at CEDAD (Centre of Applied Physics Dating and Diagnostics) at the University of Salento. Hydrogen-negative ions were produced by sputtering in a Mod. 860A ion source a TiH cathode, analyzed by a 90° bending magnet and accelerated to 3.7 MeV by a Tandetron accelerator (Mod. HVEE 4130 HC).[34] The 1H+ 3.7 MeV beam emerging from the accelerator was focused by electrostatic quadrupole lenses and transported to the external beam experimental set-up in. The beam was then collimated to 2 mm in diameter and extracted in air through a 7 µm thick Kapton extraction membrane. The beam was directed perpendicularly to the sample and the visible radiation emitted by the sample was collected in front-face geometry by an optical fiber connected to SR-2VIS400-25 Spectrometer. In order to estimate the interaction depth, the range of 3.7 MeV protons in the analyzed material was simulated by using the Stopping and Range of Ions in Matter (SRIM). In this way, a longitudinal range of 165 µm was estimated. The measurement range of the detected light was in the wavelength range from 300 to 800 nm selected by Ocean Direct Software. The acquired raw data (Integration Time (sec) were collected at 2s Scans to average: 1, Boxcar width: 10, Number of Pixels in Spectrum: 2068) were postprocessed in order to identify the spectral position of the emission peak for 5 min of scan for each sample. Characteristics X-rays emitted by the material because of inner shell atomic ionizations were also detected by means of an Silicon Drift Detector (SDD) by Amptek to ensure the stability of the beam.

2.2.6. Scintillation Kinetics with Pulsed X-Rays

The scintillation kinetics of the samples under X-rays were measured employing a TCSPC set-up described in detail in Ref.[35] A diode laser (PDL 800-B, PicoQuant) with 40 ps Full Width at Half Maximum (FWHM) pulse width drove an X-ray tube (XRT N5084, Hamamatsu) biased at 40 kV. The X-ray energy spectrum extended to 40 keV–with a peak at ≈10 keV due to L-characteristic lines of the Tungsten anode; the mean energy was ≈15 keV. The X-rays excited the sample under test on one face in a few mm region. The sample's light was collected by a Hybrid photomultiplier tube (HPM 100–07, Becker&Hickl) equipped with a band-pass filter centered at 500 with 40 nm FWHM to reduce background stray light. The sample was placed at an angle such that the HPM pointed toward the same sample's face excited by the X-rays. The impulse response function (IRF) of the set-up was obtained by convolving the IRF of the laser and the HPM measured by the authors with the IRF of the X-ray tube measured by the producer. The IRF of the set-up had a FWHM of 160 ps.

The scintillation kinetics was parameterized by a linear combination of 3 bi-exponential functions:

$$f(t/\theta) = \Theta(t-\theta)\sum_{i=1}^{3}\rho_i \cdot \frac{e^{-(t-\theta)/\tau_{d,i}} - e^{-(t-\theta)/\tau_r}}{\tau_{d,i} - \tau_r} \quad (2)$$

Being $\tau_{d,i}$, ρ_i the decay time and relative abundance of the i-th component, τ_r the rise time, and the Heaviside step function to account for the delay theta of the signal introduced by the cables. The function $f(t)$ was numerically convolved with the IRF of the set-up and fitted to the data.

A useful figure of merit in timing application, the effective decay time $\tau_{d,eff}$ was also calculated as follow:

$$\frac{1}{\tau_{d,eff}} = \frac{\rho_1}{\tau_{d,1}} + \frac{\rho_2}{\tau_{d,2}} + \frac{\rho_3}{\tau_{d,3}} \quad (3)$$

2.2.7. 3D Printing by SLA

SLA was used to 3D print models using the developed composite formulation. An Anycubic PhotonS 3D printer equipped with a 402 nm laser and a resin tank capacity of 100 mL was used. The 3D models were sliced to appropriate dimensions using Chitubox software. For the 3D printing parameters, the bottom layer exposure time was set to 80 s and the layer exposure time was set to 20 s. The thickness of each layer was set to 0.050 mm.

The composite formulation for SLA was prepared by mixing 250 mg of Cs_4PbBr_6 powder in 100 g of GDRB, in N2 atmosphere, and stirring for 1.5 h at 300 rpm to achieve a homogenous dispersion. The lowest filler content was initially selected to demonstrate the feasibility of the approach being developed.

3. Results and Discussion

The developed solvent-free composite fabrication is shown in **Figure 1**.

The incorporation of the Cs_4PbBr_6 powders into the photocurable resin provided a homogeneous composite formulation that can be processed with different techniques, from drop-casting to doctor blades to the more customizable SLA. Figure 1b illustrates the rheological measurements, which demonstrate that the Newtonian behavior exhibited by the GDRB commercial resin remains unaltered following the inclusion of Cs_4PbBr_6 powder. The viscosity values range from 0.1 Pa·s for filler loading of 1–5 wt.%, to 0.4 Pa·s for the sample containing the 10 wt.% filler, to 0.5 Pa·s as the filler loading is increased to 30 wt.%. These values are not significantly different from GDRB (0.2 Pa·s), but the influence of the Cs_4PbBr_6 on the viscosity of the resin is greater at high filler loading.

FTIR measurements were performed on GDRB and Cs_4PbBr_6 (30%)-GDRB to monitor the functional group changes in the resin after photopolymerization and to investigate if the filler has some effect on it.

As most of the commercial UV-curable formulation, GDBR is a combination of acrylic monomers and oligomers,

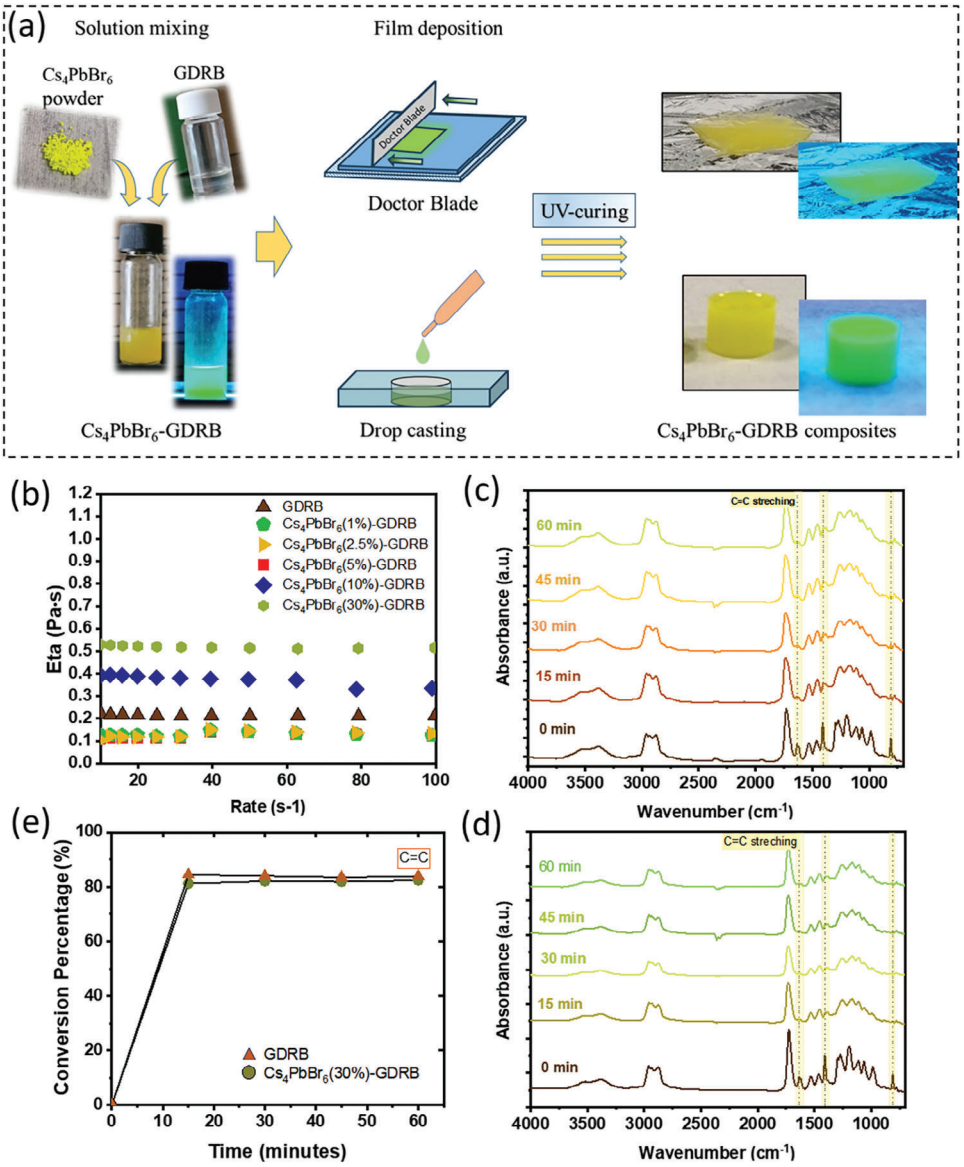

Figure 1. Composite fabrication a); Rheological measurements on Cs_4PbBr_6-GDRB composite by varying the perovskite content from 0 to 30 wt.% b); FTIR spectra of GDRB c) and Cs_4PbBr_6 (30%)-GDRB d); Conversion of C=C bonds as a function of time for GDRB and Cs_4PbBr_6 (30%)-GDRB e).

including urethane acrylate as shown in Table S1 (Supporting Information), and the photoinitiator, which are essential for radical polymerization.

FTIR measurements were taken along 60 min of UV exposure, as reported in Figure 1c,d for unfilled and 30 wt.% filled resin, respectively. The main C=C stretching peaks at 1635 and 1619 cm^{-1}, together with the peaks at 1409 and 810 cm^{-1}, typical of the acrylate group, are identified in both samples and their intensity decreased with increasing UV-curing time, due to the reduction of double bonds during chain photoactivated polymerization of acrylic moieties, irrespective to the presence of the perovskite.[36,37] Moreover, a conversion efficiency of C=C bonds ≈83% is calculated for both samples, according to Equation (1) as shown in Figure 1e, confirming that the presence of the filler does not affect the cure yield.

SEM images of deposited blade samples (reported in Figure S1a–d, Supporting Information) demonstrate a uniform distribution of perovskite in the polymer matrix, even at the higher concentration, showing powder particle size ranges from a few hundreds of nanometres to micrometers, with an average size of 1.3 ± 0.2 µm, consistent with DLS measures (Figure S1e, Supporting Information), regardless of the percentage of perovskite in the polymer matrix.

In order to investigate the printability of the formulated materials through stereolithography, it was essential to ensure that the mixtures met the requisite printing standards in terms of viscosity, photo-crosslinking rate, and stability in air. Since the phase structure of the perovskite has a direct correlation with its photophysical properties and stability in air, XRD measurements were carried out on the Cs_4PbBr_6 powder as well as on the Cs_4PbBr_6

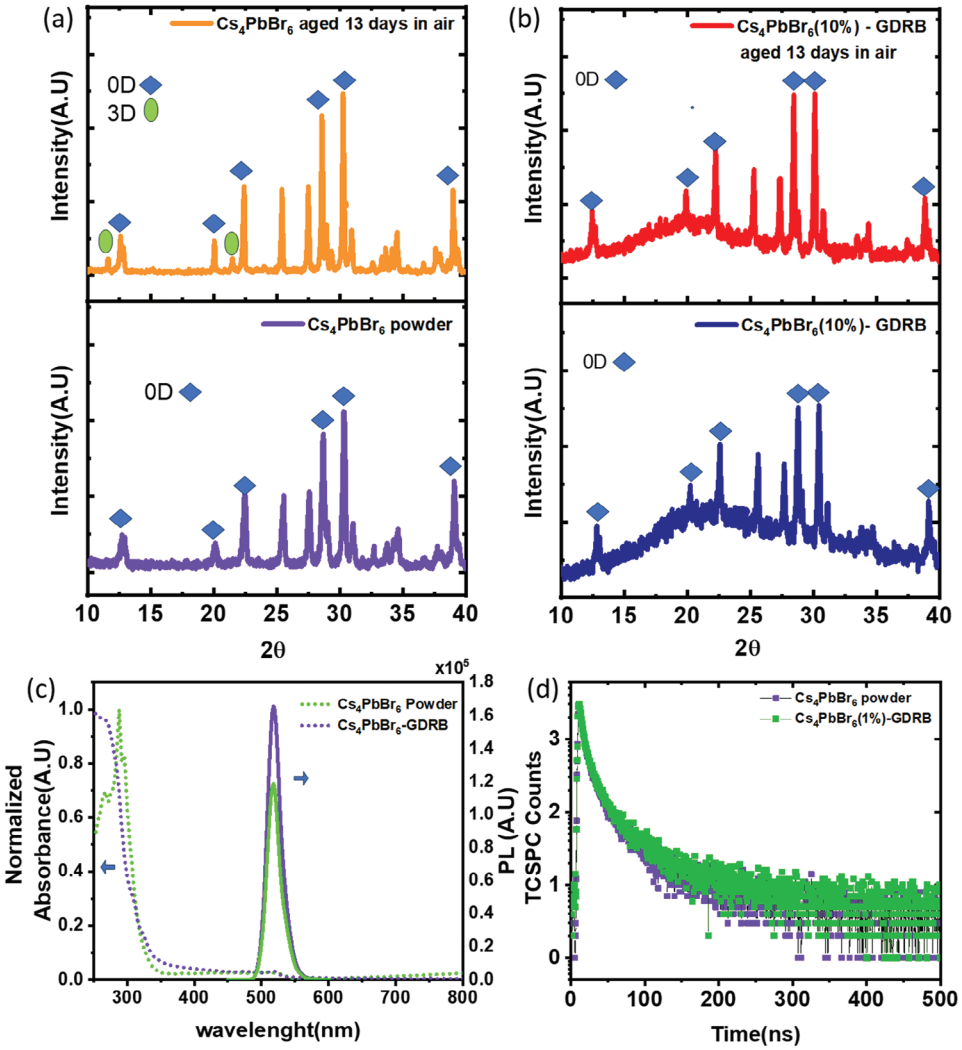

Figure 2. XRD Patterns of Cs_4PbBr_6 Powder a) and Cs_4PbBr_6 (10%)-GDRB composite b) before (bottom) and after aging in the air for 13 days (top). Absorbance and Photoluminescence spectra of the pristine powder and Cs_4PbBr_6 (1%)-GDRB c); TCSPC analysis of the powder and composite d).

(10%)-GDRB samples before and after aging in air for 13 days. It is important to note that perovskite Cs_4PbBr_6 is inherently unstable in the presence of water due to CsBr extraction in humid or aqueous environments, which ultimately leads to its conversion into $CsPbBr_3$.[38] For powder forms, this instability can result in significant variations in optical performance and a reduction in photoluminescence quantum yields (PLQYs).[32,39] As a reference, the XRD spectra of the crosslinked resin show a broad band characteristic of amorphous material (Figure S2, Supporting Information).

The comparison of XRD spectra of the perovskite powders before and after aging, shown in **Figure 2**, indicates that Cs_4PbBr_6 powder aged in air undergoes a transformation from the 0D Cs_4PbBr_6 phase to the 3D $CsPbBr_3$ crystalline phase. The latter must be considered as $CsPbBr_3$ impurities corresponding to peaks at 11.5° and 21.5° in the XRD spectra of the Cs_4PbBr_6 powder (Figure 2a). On the contrary, Cs_4PbBr_6 (10%)-GDRB does not show the 3D $CsPbBr_3$ phase of Cs_4PbBr_6 after aging (Figure 2b). This important result indicates that a high stability of the perovskite is achieved when embedded in the resin, which could be considered a fundamental requirement for assessing the printability of the composite formulation by SLA in air.[40,41]

For the development of scintillator devices, the transparency of GDRB-based composites is crucial in order to avoid self-absorption of the luminescence feature of the perovskite filler. In our case, the resin absorbs in the UV region and does not emit in the visible spectrum (Figure 2c). The Cs_4PbBr_6 powder is characterized by two peaks in the absorption spectra: the first one at 300 nm, attributed to the pure Cs_4PbBr_6 phase, and the second one at 520 nm attributed to bromide vacancies or impurities with 3D-like structure, which are responsible for the emission at 520 nm. This characteristic defect tolerance makes it a promising candidate for radiation detection.[21,24,42] Furthermore, upon insertion of the powder at varying percentages, no discernible shift or broadening in the emission peak is observed (λem = 520 nm, FWHM = 23 nm). To corroborate this result, also the TCSPC analysis (Figure 2d) showed no change in the lifetime resulting in an average lifetime of 46 ns with a

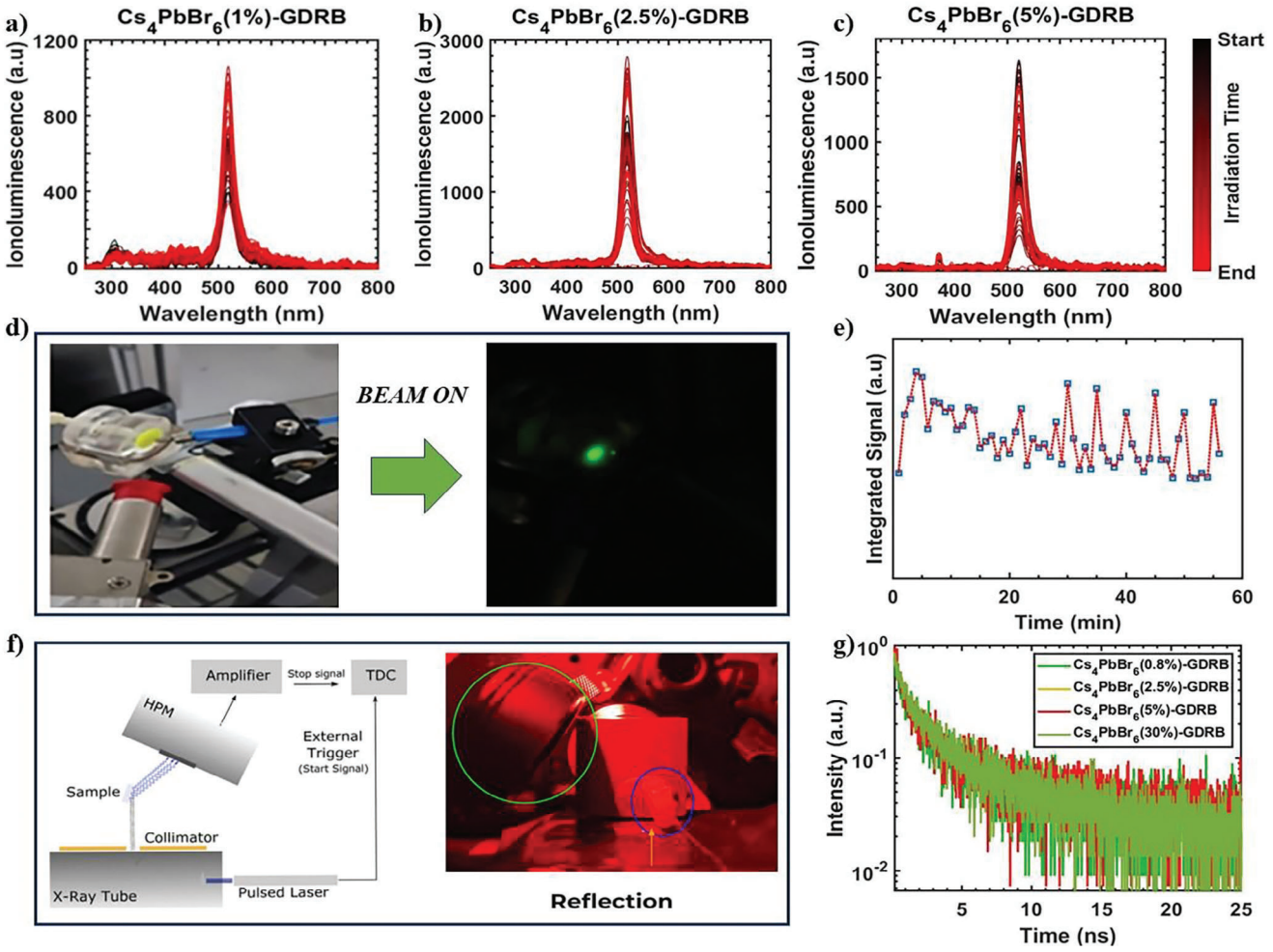

Figure 3. Scintillation Analysis: Ibil spectra of Cs_4PbBr_6 (1%)-GDRB a), Cs_4PbBr_6 (2.5%)-GDRB b) and of Cs_4PbBr_6 (5%)-GDRB c). Photograph of the Ibil experimental set-up, Cs_4PbBr_6 (2.5%)-GDRB composite disk before and during the proton beam turning on d). Radiation Hardness test: integrated Ionoluminescence peak during time (min) e) Photograph of the scintillation test setup f) Scintillation time-profile of the samples from 0.8 wt.% Cs_4PbBr_6 loading to 30 wt.% g).

three-exponential fit, whose results are detailed in Table S2 (Supporting Information).

With the aim of increasing the harvesting of the radiation, 2 mm thick cylinder-shaped samples were fabricated with increased Cs_4PbBr_6 powder loading from 1% to 5% (Figure S3a, Supporting Information). These samples show increased photoluminescence and a decrease in transmittance due to the increased concentration of perovskite (Figure S3a,b, Supporting Information).

The emission properties of the developed samples reported in **Figure** 3a–c were characterized under proton irradiation by using the experimental setup depicted in Figure 3d. The maximum of the emission peak was at 520 nm, without shift when compared with the PL spectra. As expected, there was an increase in luminescence counts as a function of the perovskite concentration for 1% and 2.5% and a reduction of the count for the 5% due probably to a Pl-quenching phenomena and a poor transmittance of the sample. Furthermore, there was a fluctuation of the peak as a function of the scanning time, due to the instability of the beam when extracted in air. To prove this, it was decided to halve the current and place the sample with 2.5% loading at a prolonged irradiation time as depicted in Figure 3e. Indeed, it can be seen that there is an excellent radiation hardness with only a slight decrease in the counts over time. The points were the integrated signal below the curve at each scan.

The TCSPC measurements with a pulsed X-ray source, reported in Figure 3g as varying the Cs_4PbBr_6 loading from 0.8 to 30 wt.%, show visibly fast scintillation. The sample with 2.5 wt.% loading and the pure GDRB (0 wt.% loading) were measured for ≈15 h and the results are rescaled for comparison and plotted in Figure S4 (Supporting Information).

The fit results for all the samples are reported in **Table** 2. Within the experimental precision, all showed compatible scintillation characteristics, best described by 3 decay components: the first of ≈100 ps accounting for 8–9% of the emitted light; the second of 2 ns (30–45%); the third of 20 ns. The rise time was below 20 ps, the resolution limit of the set-up. An effective decay time of ≈1.0 ± 0.2 ns was calculated, demonstrating a kinetic response comparable to that of ultra-fast scintillating materials.[35,43,44] Preliminary performance measurements gave a light yield of ≈10%

Table 2. Fit results of the scintillation kinetics measurements with pulsed X-rays. The experimental uncertainty on the decay times is 5%; on the rise time, 20 ps; on the effective decay time, ±0.2 ns.

Loading	Rise time [ps]	Decay time 1 [ns]	%	Decay time 2 [ns]	%	Decay time 3 [ns]	%	Effective decay time [ns]
Set 1–0.8 wt.%	2	0.10	8.1	2.0	42.7	23	49.2	1.0
Set 1–2.5 wt.%	2	0.10	8.7	1.9	36.1	19	55.3	0.9
Set 1–5.0 wt.%	1	0.10	9.0	1.9	35.6	22	55.4	0.9
Set 1–30 wt.%	1	0.10	6.8	2.0	44.8	17	48.4	1.1

of a commercial EJ232 scintillator. This value is likely due to the particle size and dispersion of the perovskite powder in the composite, which was selected for its ease of synthesis, stability, and low cost.

Finally, the successful stereolithography printability of the selected Cs_4PbBr_6 (0.25)-GDRB composite formulation was demonstrated, as shown in **Figure 4**. The printing of the high-quality prototypes with complex geometries, whose respective 3D printed models are shown in Figure 4, was achieved after proper optimization of the process parameters (Table S3) by using a simple, accurate, and economical process in a very short time (1 h 20 min).

This important result represents a proof-of-concept of the first 3D-printed fast scintillators demonstrating the feasibility of our developed approach. The inclusion of perovskite fillers does not influence the rheological and photo-curing behavior during the SLA printing process, while at the same time ensuring improved stability in ambient air and a fast kinetic response of the 3D plastic printed scintillator. Finally, we also demonstrated that 3D printing offers the possibility to easily customize prototypes (as can be seen in Figure 4). Each piece can be modified to meet specific needs, for definite applications, without incurring significant additional costs. This is particularly useful for the production of plastic scintillators.

4. Conclusion

A photopolymerisable composite consisting of a photocurable resin and Cs_4PbBr_6 perovskite powders was first developed to fabricate ultra-fast plastic scintillators with complex geometries using stereolithography. This composite was effectively 3D printed, resulting in plastic scintillators with intricate designs and high resolution. The use of high-Z lead-based perovskite fillers ensured the detection of ionizing radiation and its conversion into visible light without affecting the resin's rheological and photocuring behavior, while the polymer matrix facilitated the printability of the customized composite. Overall, the presence of the polymer matrix ensured improved filler stability in ambient air without compromising the ultra-fast response to

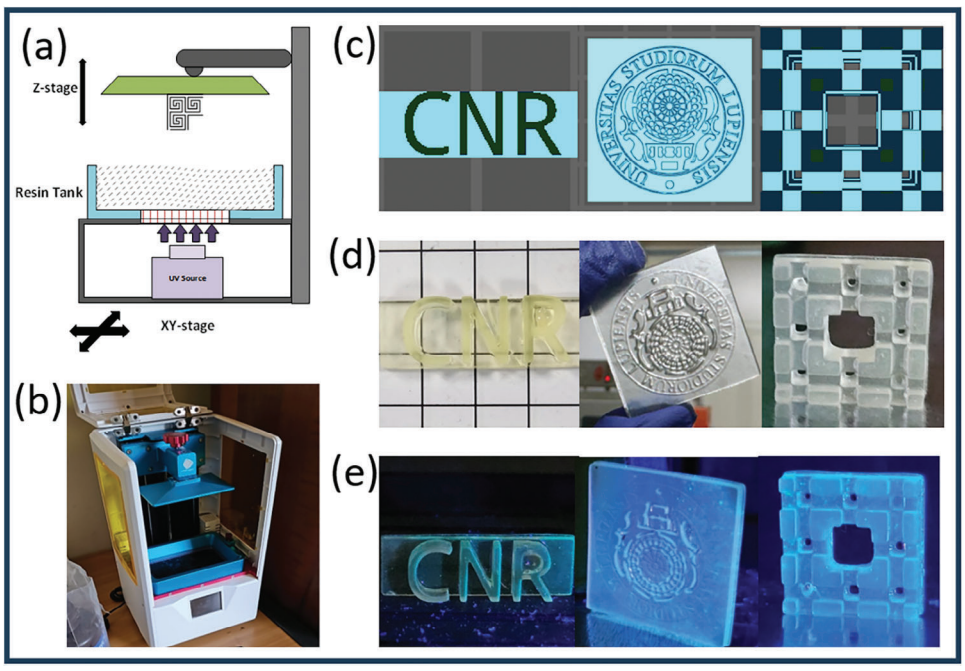

Figure 4. SLA with composite formulation Cs_4PbBr_6 (0.25)-GDRB a) SLA apparatus (with 6bottom-up configuration.) b) AnyCubic PhotonS 3D-printer c) CAD models d) 3D-printed objects before and under UV irradiation e).

irradiation exhibited by the scintillating filler, showing an effective decay time of ≈1.0 ± 0.2 ns. Preliminary comparison of the performance of the developed scintillator gave a light yield of ≈10% of a commercial EJ232 scintillator, likely due to the perovskite powder size and dispersion in the composite, which however was selected for its ease of synthesis, stability, and low cost.

This work, thus, paves the way for the development of an entirely new class of plastic scintillating materials that can be used to build radiation detectors to be used in intensity-modulated and volume-modulated therapies for high conformity. The preliminary results of this work have, in fact, shown that the use of 3D printing technology for the prototyping of scintillators offers numerous advantages, including process simplicity, the ability to create complex geometries with precision and accuracy, cost-effectiveness, reduction of production times and customization possibilities. These benefits make 3D printing an excellent choice for anyone looking to develop high-quality prototypes efficiently and effectively.

This study serves as a proof of concept, demonstrating the potential to fabricate fast perovskite-based scintillators with complex shapes using additive manufacturing (AM). Further work is in progress to improve the transparency and light yield of the 3D perovskite-based composite scintillators.

Supporting Information

Supporting Information is available from the Wiley Online Library or from the author.

Acknowledgements

The research activities leading to this work were supported by the National Institute of Nuclear Physics_INFN (SHINE project). A.G and A.R. acknowledge PNRR MUR project: "Integrated Infrastructure Initiative in Photonic and Quantum Sciences"–I-PHOQS (IR0000016). The authors gratefully acknowledge Donato Cannoletta for SEM Analysis.

Open access publishing facilitated by Consiglio Nazionale delle Ricerche, as part of the Wiley - CRUI-CARE agreement.

Conflict of Interest

The authors declare no conflict of interest.

Data Availability Statement

The data that support the findings of this study are available from the corresponding author upon reasonable request.

Keywords

3D Printed scintillators, photocurable polymer composite, ultra-fast Plastic Scintillators

Received: September 20, 2024
Revised: November 20, 2024
Published online:

[1] C. Dujardin, E. Auffray, E. Bourret-Courchesne, P. Dorenbos, P. Lecoq, M. Nikl, A. N. Vasil'Ev, A. Yoshikawa, R. Y. Zhu, *IEEE Trans. Nucl. Sci.* **2018**, *65*, 1977.
[2] A. Pietropaolo, M. Angelone, R. Bedogni, N. Colonna, A. J. Hurd, A. Khaplanov, F. Murtas, M. Pillon, F. Piscitelli, E. M. Schooneveld, K. Zeitelhack, *Phys. Rep.* **2020**, *875*, 1.
[3] C. W. E. Van Eijk, *IOP Sci.* **2002**, *47*, R85.
[4] J. B. Birks, *The Theory and Practice of Scintillation Counting: International Series of Monographs in Electronics and Instrumentation*, Elsevier, Amsterdam **2013**.
[5] Z. Lin, S. Lv, Z. Yang, J. Qiu, S. Zhou, *Adv. Sci.* **2022**, *9*, 2102439.
[6] Y. Zhou, J. Chen, O. M. Bakr, O. F. Mohammed, *ACS Energy Lett.* **2021**, *6*, 739.
[7] O. D. I. Moseley, T. A. S. Doherty, R. Parmee, M. Anaya, S. D. Stranks, *J Mater Chem C Mater* **2021**, *9*, 11588.
[8] G. F. Knoll, *Radiation Detection and Measurement*, John Wiley & Sons, Hoboken, NJ **2010**.
[9] G. H. V. Bertrand, M. Hamel, S. Normand, F. Sguerra, *Nucl. Instrum. Methods Phys. Res. A* **2015**, *776*, 114.
[10] S. Berns, A. Boyarintsev, S. Hugon, U. Kose, D. Sgalaberna, A. De Roeck, A. Lebedynskiy, T. Sibilieva, P. Zhmurin, *J. Instrument.* **2020**, *15*, P10019.
[11] N. Suchaworska, P. Z. Y. Liu, A. Ralston, P. Naseri, P. Abolfathi, J. Lee, K. Warrener, D. R. McKenzie, *J. Phys. Conf. Ser.* **2013**, *444*, 012075.
[12] I. I. Tendler, P. Bruza, M. Jermyn, A. Fleury, B. B. Williams, L. A. Jarvis, B. W. Pogue, D. J. Gladstone, *J. Biomed. Opt.* **2019**, *24*, 1.
[13] M. Rahman, P. Brža, K. M. Langen, D. J. Gladstone, X. Cao, B. W. Pogue, R. Zhang, *Phys. Med. Biol.* **2020**, *65*, 165014.
[14] N. Lynch, T. Monajemi, J. L. Robar, *Biomed. Phys. Eng. Express* **2020**, *6*, 055014.
[15] P. Stowell, Z. Kutz, S. Fargher, L. F. Thompson, *J. Instrum.* **2021**, *16*, P01003.
[16] C. Liu, Z. Li, J. Hajagos, D. Kishpaugh, D. Y. Chen, Q. Pei, *ACS Nano* **2017**, *11*, 6422.
[17] M. Cao, C. Hu, E. Wang, *J. Am. Chem. Soc.* **2003**, *125*, 11196.
[18] S. R. Sandler, K. C. Tsou, *Int. J. Appl. Radiat. Isot.* **1964**, *15*, 419.
[19] J. Perego, I. Villa, A. Pedrini, E. C. Padovani, R. Crapanzano, A. Vedda, C. Dujardin, C. X. Bezuidenhout, S. Bracco, P. E. Sozzani, A. Comotti, L. Gironi, M. Beretta, M. Salomoni, N. Kratochwil, S. Gundacker, E. Auffray, F. Meinardi, A. Monguzzi, *Nat. Photonics* **2021**, *15*, 393.
[20] V. S. D. Voet, T. Strating, G. H. M. Schnelting, P. Dijkstra, M. Tietema, J. Xu, A. J. J. Woortman, K. Loos, J. Jager, R. Folkersma, *ACS Omega* **2018**, *3*, 1403.
[21] Q. Chen, J. Wu, X. Ou, B. Huang, J. Almutlaq, A. A. Zhumekenov, X. Guan, S. Han, L. Liang, Z. Yi, J. Li, X. Xie, Y. Wang, Y. Li, D. Fan, D. B. L. Teh, A. H. All, O. F. Mohammed, O. M. Bakr, T. Wu, M. Bettinelli, H. Yang, W. Huang, X. Liu, *Nature* **2018**, *561*, 88.
[22] A. Wibowo, M. A. K. Sheikh, L. J. Diguna, M. B. Ananda, M. A. Marsudi, A. Arramel, S. Zeng, L. J. Wong, M. D. Birowosuto, *Commun. Mater.* **2023**, *4*, 21.
[23] M. L. Zaffalon, F. Cova, M. Liu, A. Cemmi, I. Di Sarcina, F. Rossi, F. Carulli, A. Erroi, C. Rodà, J. Perego, *Nat. Photonics* **2022**, *16*, 860.
[24] M. Gandini, I. Villa, M. Beretta, C. Gotti, M. Imran, F. Carulli, E. Fantuzzi, M. Sassi, M. Zaffalon, C. Brofferio, L. Manna, L. Beverina, A. Vedda, M. Fasoli, L. Gironi, S. Brovelli, *Nat. Nanotechnol.* **2020**, *15*, 462.
[25] K. Děcká, F. Pagano, I. Frank, N. Kratochwil, E. Mihóková, E. Auffray, V. Čuba, *J. Mater. Chem. C Mater.* **2022**, *10*, 12836.
[26] A. Anand, M. L. Zaffalon, A. Erroi, F. Cova, F. Carulli, S. Brovelli, *ACS Energy Lett.* **2024**, *9*, 1261.
[27] J. Huang, Q. Qin, J. Wang, *Processes* **2020**, *8*, 1138.
[28] G. N. Mhetre, V. S. Jadhav, S. P. Deshmukh, C. M. Thakar, *ECS Trans.* **2022**, *107*, 15355.
[29] G. Rasiya, A. Shukla, K. Saran, *Mater. Today Proc* **2021**, *47*, 6896.

[30] X. Liu, W. Xie, Y. Lu, X. Wang, S. Xu, J. Zhang, *J. Mater. Chem. C Mater.* **2022**, *10*, 762.
[31] A. Ray, D. Maggioni, D. Baranov, Z. Dang, M. Prato, Q. A. Akkerman, L. Goldoni, E. Caneva, L. Manna, A. L. Abdelhady, *Chem. Mater.* **2019**, *31*, 7761.
[32] M. I. Saidaminov, J. Almutlaq, S. Sarmah, I. Dursun, A. A. Zhumekenov, R. Begum, J. Pan, N. Cho, O. F. Mohammed, O. M. Bakr, *ACS Energy Lett.* **2016**, *1*, 840.
[33] H. Zhang, Q. Liao, Y. Wu, J. Chen, Q. Gao, H. Fu, *Phys. Chem. Chem. Phys.* **2017**, *19*, 29092.
[34] F. Kotz, P. Risch, D. Helmer, B. E. Rapp, *Micromachines (Basel)* **2018**, *9*, 30115.
[35] F. Pagano, N. Kratochwil, I. Frank, S. Gundacker, M. Paganoni, M. Pizzichemi, M. Salomoni, E. Auffray, *Front. Phys.* **2022**, *10*, 1021787.
[36] K. T. Teo, A. Hassan, S. N. Gan, *Polymers (Basel)* **2018**, *10*, 1374.
[37] D. Kunwong, N. Sumanochitraporn, S. Kaewpirom, *Sonkl. J. Sci. Technol.* **2011**, *33*, 201.
[38] L. Wu, H. Hu, Y. Xu, S. Jiang, M. Chen, Q. Zhong, D. Yang, Q. Liu, Y. Zhao, B. Sun, Q. Zhang, Y. Yin, *Nano Lett.* **2017**, *17*, 5799.
[39] Y. Rakita, N. Kedem, S. Gupta, A. Sadhanala, V. Kalchenko, M. L. Böhm, M. Kulbak, R. H. Friend, D. Cahen, G. Hodes, *Cryst. Growth Des.* **2016**, *16*, 5717.
[40] L. Wu, H. Hu, Y. Xu, S. Jiang, M. Chen, Q. Zhong, D. Yang, Q. Liu, Y. Zhao, B. Sun, *Nano Lett.* **2017**, *17*, 5799.
[41] Q. A. Akkerman, S. Park, E. Radicchi, F. Nunzi, E. Mosconi, F. De Angelis, R. Brescia, P. Rastogi, M. Prato, L. Manna, *Nano Lett.* **2017**, *17*, 1924.
[42] D. N. Dirin, L. Protesescu, D. Trummer, I. V. Kochetygov, S. Yakunin, F. Krumeich, N. P. Stadie, M. V. Kovalenko, *Nano Lett.* **2016**, *16*, 5866.
[43] Y. Tang, G. Pu, Y. Tang, T. Sun, M. Wang, J. Wang, *J. Phys. Chem. Lett.* **2024**, *15*, 7036.
[44] S. Gundacker, R. M. Turtos, N. Kratochwil, R. H. Pots, M. Paganoni, P. Lecoq, E. Auffray, *Phys. Med. Biol.* **2020**, *65*, 025001.